Joule

CellPress

Article

Mobile Ion Concentration Measurement and Open-Access Band Diagram Simulation Platform for Halide Perovskite Solar Cells

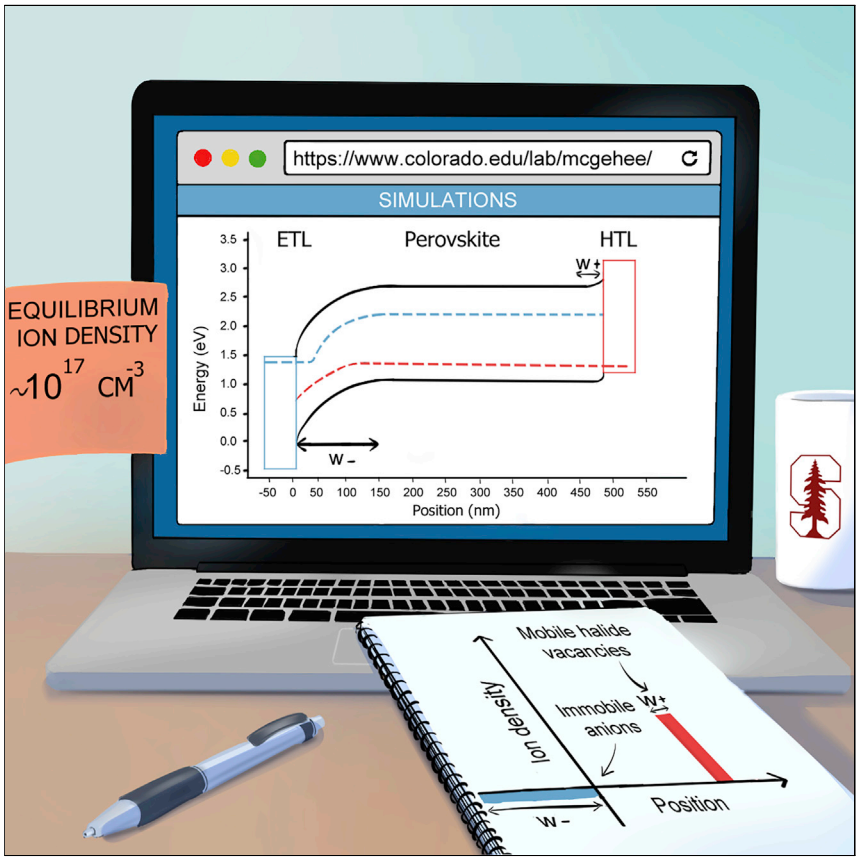

Halide vacancies have been suggested to be the prevalent mobile ionic species in mixed ionic-electronic perovskite solar cells. In this paper, we measure the concentration of these vacancies. We also model the ionic-electronic transport properties of these devices and provide an online platform to allow anyone to understand the device physics of their own solar cells. We show that mobile ions have no impact on highly efficient devices but can reduce the efficiency of less-than-20%-efficient solar cells.

Luca Bertoluzzi, Caleb C. Boyd, Nicholas Rolston, Jixian Xu, Rohit Prasanna, Brian C. O'Regan, Michael D. McGehee

lbertoluzzi@gmail.com (L.B.)
michael.mcgehee@colorado.edu (M.D.M.)

HIGHLIGHTS

Perovskite solar cells with mobile ions and p-n junctions have analogous band diagrams

The mobile vacancy density for various mixed halide perovskites is $\sim 10^{17} cm^{-3}$

Mobile ion densities $\lesssim 10^{15}$ cm^{-3} are beneficial for $\lesssim 20$ % efficient devices

Simulations explain why n-i-p devices are more efficient than p-i-n devices

Bertoluzzi et al., Joule 4, 109–127
January 15, 2020 Published by Elsevier Inc.
https://doi.org/10.1016/j.joule.2019.10.003

Joule

CellPress

Article

Mobile Ion Concentration Measurement and Open-Access Band Diagram Simulation Platform for Halide Perovskite Solar Cells

Luca Bertoluzzi,[1,*] Caleb C. Boyd,[1,2] Nicholas Rolston,[3] Jixian Xu,[1,2] Rohit Prasanna,[1,2] Brian C. O'Regan,[4] and Michael D. McGehee[2,5,6,*]

SUMMARY

We propose two approaches to compute the band diagram of highly efficient perovskite solar cells, both based on the migration of a single-mobile ion (halide vacancies). The first is a full analytical approach to quickly calculate the main features of the perovskite band diagram and easily extract the mobile vacancy concentration from experimental data. The second approach is an online-open-access platform that can be used by anyone to accurately simulate their own band diagram. We combine the first approach with current transient measurements to extract the mobile ion concentration for six different perovskite compositions—including perovskite solar cells with power conversion efficiencies exceeding 19%. For the devices measured herein, we obtain ion concentrations in the range 7×10^{16}–5×10^{17} cm^{-3}. We use the second approach to quantitatively discuss the implications of the mobile ion concentrations we measured in terms of device performance and stability.

INTRODUCTION

With the recent announcement of 28% efficient perovskite-silicon tandem solar cells by Oxford PV, halide perovskites have confirmed their ability to enhance the most efficient single-junction silicon solar cells in addition to producing 25.2% efficient single-junction devices.[1] However, the analysis of this technology's working principles can be blurred by substantial densities of mobile ions in these mixed ionic-electronic semiconductors. In fact, mobile ions modulate the electric field and charge carrier distribution within the perovskite absorber.[2] Both quantities directly affect the solar device optoelectronic properties (bulk/interfacial carrier recombination and transport),[3] mechanical properties (compressive film strain),[4,5] and photovoltaic behavior (reverse bias breakdown,[6] photo-induced halide segregation,[7,8] hysteresis,[9] degradation[10] etc.). Understanding this technology, therefore, requires computing an accurate band diagram (energy versus position) that accounts for a distribution of electric field in perovskite solar cells that is consistent with experimental results.

Two main features of the electric field distribution have been experimentally unveiled in perovskite devices. The electric field is (1) shielded in bulk and (2) distributed asymmetrically within the absorber. The first piece of evidence is the observation of a negative photocurrent opposite to the photocurrent induced by carrier extraction right after applying a forward voltage (i.e., a negative field) to a device initially at equilibrium.[11–14] To explain this observation, it has been proposed that the positive built-in voltage drops at the contacts and is zero in the bulk at

Context & Scale

Halide perovskites are mixed ionic-electronic semiconductors with extraordinary optoelectronic properties. To fully understand perovskite solar cells, it is crucial to accurately quantify the distribution of mobile ions and assess their impact on the device band diagram. Accurate knowledge of the band diagram is critical to calculate carrier mobilities, hysteresis, degradation, electrostriction, and carrier tunneling at reverse bias. However, perovskite solar cell band diagrams are usually computed fully or semi-numerically and require in-depth knowledge of drift-diffusion simulations and costly simulation software. As a result, accurate band diagrams are rarely used to optimize perovskite devices. In this work, we present approximations that simplify band diagram calculations, provide a free online device simulator, and discuss important conclusions that can be drawn from the analysis of perovskite band diagrams with different mobile ion densities and direction of illumination.

equilibrium. Hence, the negative applied field creates a net negative field in the bulk that drives most photogenerated carriers away from their selective contacts and leads to a negative photocurrent (see Figures S1A and S1B). The second piece of experimental evidence is the observation of reverse bias breakdown currents for relatively small reverse bias values (between −1 and −5 V).[6] This behavior has been ascribed to carrier tunneling from the perovskite into one of the transport layers (see Figures S1C and S1D). This only occurs when most of the voltage within the absorber drops close to one of the contacts, allowing for a thin tunneling barrier.[6] Most of the potential dropping close to one contact implies that the field is distributed asymmetrically and suggests that the bulk is field-free at steady state. The last piece of evidence is that provided by Weber et al.[15] These authors revealed an asymmetric potential distribution within the perovskite absorber using Kelvin probe force microscopy (KPFM) after applying 0.5 V in the dark. They showed that after 700 ms, ~80% of the applied voltage drops close to the electron transport layer (ETL), and the remaining ~20% drops close to the hole transport layer (HTL), leaving no voltage drop within the bulk.

To compute a band diagram that accurately reproduces both electric field features afore introduced, it is crucial to know the mobile ion distribution within the absorber and their concentration. To date, most studies suggest that ionic transport is mostly mediated through halide vacancies (V_X^+)[16–20] that are compensated by much slower negatively charged vacancies such as V_{MA}^-, V_{Pb}^-, etc. (Schottky disorder)[21] or by halide interstitials, X_i^- (Frenkel pairs).[22,23] The published concentrations of halide vacancies measured or theoretically predicted with density functional theory for different compositions vary widely between 10^{15} and 10^{19} cm^{-3}.[14,15,21,24,25] Note that some studies suggest the presence of other types of ions such as MA^+,[26,27] or H^+,[28] with smaller concentrations ($\lesssim 10^{15}$ cm^{-3}). Since the electric field is controlled by the ions with the highest concentrations, we will not consider these ions in the rest of this paper. Recent reports also suggest that other types of mobile ions might be involved under prolonged illumination.[10,29,30] However, in this paper we study the electric field and mobile ion distribution prior to any long-term photo-induced process.

While the literature indicates that halide vacancies are the prevalent mobile ions in most perovskite solar cells, the wide range of experimental and theoretical concentration values reported in the literature for similar devices (10^{15}–10^{19} cm^{-3})[14,15,21,24,25] suggests that there is no clear consensus on the value of the mobile vacancy concentration in these devices. Some of this variation in reported vacancy concentrations is likely due to the use of different models and different assumptions. Therefore, it is crucial to revisit the assumptions of these models and establish a general theory that allows to consistently, easily, and accurately measure the ion concentrations for multiple perovskite compositions and device architectures. Once the mobile ion concentration has been measured, the device band diagram can be simulated either with an analytical model or by full drift-diffusion simulations. On the first hand, the full analytical approach is very useful to quickly understand the device physics of perovskite devices. However, to the best of our knowledge, no full analytical derivation has been proposed to calculate the band diagram of perovskite solar cells. On the other hand, the full numerical approach is very useful to quantitatively discuss the potential and carrier distributions in perovskite solar cells but requires some specific computational knowledge and/or costly simulation software. This type of resource is only limited to a few groups within the community, and the use of accurate band diagrams to optimize perovskite devices is still very rare. Hence, the introduction of an

[1]Department of Materials Science and Engineering, Stanford University, Stanford, CA 94305, USA

[2]National Renewable Energy Laboratory, Golden, CO 80401, USA

[3]Department of Applied Physics, Stanford University, Stanford, CA 94305, USA

[4]Sunlight Scientific, 1190 Oxford Street, Berkeley, CA 94707, USA

[5]Department of Chemical and Biological Engineering, University of Colorado, Boulder, 80303, CO, USA

[6]Lead Contact

*Correspondence: lbertoluzzi@gmail.com (L.B.), michael.mcgehee@colorado.edu (M.D.M.)

https://doi.org/10.1016/j.joule.2019.10.003

open-access, easy-to-use-platform to simulate the band diagram of perovskite devices can serve as a useful toolkit that enables accessibility and informs experimental design for researchers.

In this paper, we first revisit the analytical models that are conventionally used to measure mobile ion concentrations and the main features of the perovskite solar cell band diagram considering the recent experimental observations previously discussed. We show that some of these models cannot explain the field distribution previously explained, while the others do not accurately capture the main band diagram features. We subsequently provide a general analytical model that depends on three degrees of freedom: the vacancy concentration, the dielectric constant, and the built-in potential. Our analytical model allows us to easily extract the mobile ion concentration and the main features of the band diagram in perovskite devices with different compositions including highly efficient devices with power conversion efficiencies >19%. We validate our approach by comparing our analytical calculations to full drift-diffusion simulations obtained with our newly designed open-access simulation platform. Our simulation platform can be used by anyone to accurately and swiftly simulate their own band diagram for various perovskite materials, contacts, ion concentrations, applied voltages, and illumination intensities.[31] Finally, we discuss important examples showing the implications of mobile ion accumulation at the contacts for the device architecture and performance.

RESULTS

Modeling Framework

Let us start by establishing the general framework that will be used throughout the rest of this paper. First, we consider an intrinsic perovskite semiconductor in the dark without any contact (Figure 1A). All the ionic species are distributed homogenously in the film with a concentration N_0 (in cm^{-3}). We then contact the film with an ETL on the left (x = 0) and an HTL on the right (x = L). Both transport layers are assumed to be heavily doped so that no voltage drops within the contacts. We will further discuss this hypothesis later in this paper. The built-in voltage resulting from the difference in contact work functions drops linearly between the HTL and ETL (Figure 1B). The built-in field triggers the migration of positively charged halide vacancies toward the HTL. This process induces the formation of a halide-vacancy-depleted region close to the ETL containing an excess of anions (Figures 1C and 1D). Note that if negatively charged mobile halides migrated instead of positively charged halide vacancies, the halide-depleted region would be formed close to the HTL and the halide-accumulation region would be created close to the ETL.

The goal of the models discussed hereafter is to quantify the vacancy concentration and compute the electric field distribution (i.e., the band diagram) within the absorber after vacancy migration. Since the mobile ion concentration is measured by applying a field between the two electrodes of a solar cell, we model the distribution of the average electric field within the whole device. We consider a continuous and uniform distribution of ions and neglect the local variations due to inhomogeneities such as grain boundaries or local ionic defects. This method avoids considering the specifics of the different perovskite morphologies and is computationally efficient. This approach is supported by the recent KPFM results of Weber et al.,[15] who showed a field profile without inhomogeneities at the nanoscale.

The following models assume that the field is governed by mobile ions only given that N_0 exceeds the carrier density under operational conditions ($\sim 10^{16} cm^{-3}$).[32]

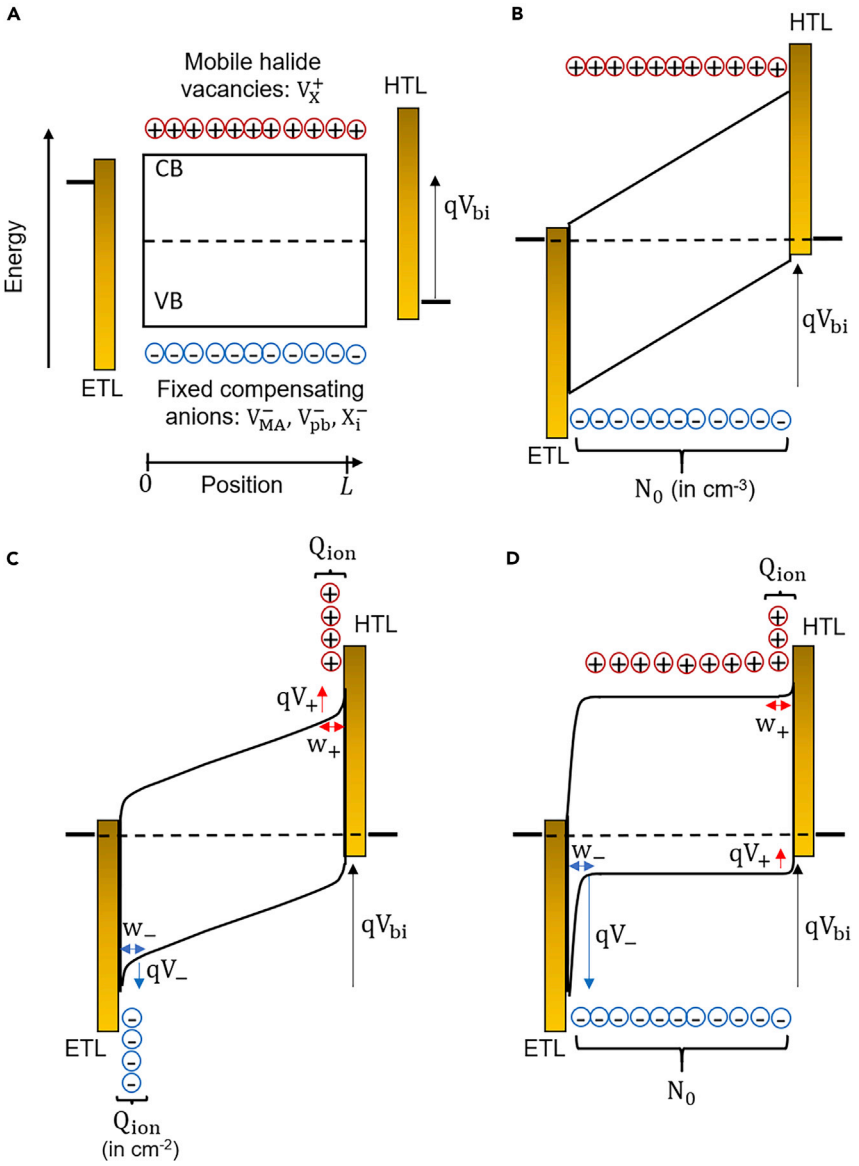

Figure 1. Schematic Energy Diagrams of an Intrinsic Perovskite Film in Dark Equilibrium

(A)The film does not have contacts. Mobile halide vacancies and compensating anions are distributed uniformly through the film with a density N_0 (in cm^{-3}).

(B) After the ETL and HTL have been deposited on either side of the film, a built-in potential (V_{bi}) is created that linearly drops within the film and triggers the drift of mobile ions toward the contacts.

(C) Case where both cations and anions are mobile. Both ions are symmetrically distributed within Debye layers, as described by the Gouy-Chapman and Debye theories (Equations 3,4, and 5).

(D) Case where halide vacancies are mobile and anions are immobile. This theory predicts an asymmetric ion distribution.

We neglect volume exclusion effects due to large ion concentrations at the interface and interfacial dipoles (this includes double layer effects). We define w_+, w_-, V_+, and V_- to be the width and voltage drops within the vacancy-accumulation (+) and vacancy-depleted (–) regions. We choose the convention: $V_+ > 0$ and $V_- < 0$. We define Q_{ion} to be the total ionic charge (in $C.cm^{-2}$) in the vacancy-depleted and vacancy-accumulation regions.

To measure N_0 and calculate the main features of the band diagram (w_+, w_-, V_+, and V_-), it is common to measure Q_{ion} and recover N_0, w_+, w_-, V_+, and V_- from a model that connects these quantities. Such a relation is obtained by solving the Poisson equation in the perovskite absorber. The Poisson equation relates the electrostatic potential field, ϕ, to the distribution of charged species. As previously mentioned, the prevailing charged species in the perovskite absorber are mobile vacancies with density n_{vac} that are compensated by anions with density n_a. Hence, the general Poisson equation reads:

$$\frac{\partial^2\phi}{\partial x^2} = -\frac{q}{\epsilon_0\epsilon_r}(n_{vac}(x) - n_a(x)), \qquad \text{(Equation 1)}$$

where q is the electron charge, ϵ_0 and ϵ_r are the dielectric constant of the vacuum and the material relative permittivity, respectively, and ϕ is related to the electric field, E, as follows:

$$E = -\frac{\partial\phi}{\partial x}. \qquad \text{(Equation 2)}$$

Conventional Analytical Models to Measure the Ion Concentration and Band Diagram Features

Two types of approaches can be found in the literature to solve Equations 1 and 2 and obtain an analytical relation between Q_{ion} and N_0, w_+, w_-, V_+, and V_-. The first considers two mobile ions of opposite charge with the same concentration, while the second accounts for one single type of mobile ion. These two cases are good approximations to model ionic transport with any number of distinct mobile ions. In fact, in the case of multiple mobile ions with the same charge (e.g., MA^+ and V_I^+), the electric field distribution would be the same as that of a single type of mobile ion ($MA^+$and V_I^+ are electrostatically equivalent). In the case of multiple mobile ions with different charges, the ion with the highest concentrations determines the electric field profile, and the absorber is electrostatically equivalent to a one-ion model. On the contrary, if the concentration of mobile cations and anions is similar, the perovskite absorber is equivalent to a two-mobile ion absorber. In the following, we briefly explain the hypotheses and main equations of each model. The full derivation can be found in the Supplemental Experimental Procedures.

The first approach assumes that the compensating anions are mobile and accumulate close to the ETL just like halide vacancies accumulate close to the HTL (Figure 1C).[30,33] In this case, all the mobile ions accumulate at the contacts and the bulk is depleted of mobile ions. Hence, the potential drops linearly within the bulk of the absorber and drops symmetrically at the contacts. The ionic charge accumulating at each contact can be obtained by integrating Equations 1 and 2 (see Supplemental Experimental Procedures). This approach—also known as the Gouy-Chapman theory—leads to the following expression of the ionic charge at the contacts[34]:

$$Q_{2\ ions}^{G-C} = 2\frac{\epsilon_0\epsilon_r V_T}{L_D}\sinh\left(\frac{V}{2V_T}\right), \qquad \text{(Equation 3)}$$

where V is the voltage drop within each accumulation region, V_T is the thermal voltage (V_T = 26 mV at 25 °C) and L_D is the Debye length, which is an estimate for the accumulation region width:

$$L_D = \sqrt{\frac{\epsilon_0\epsilon_r V_T}{2qN_0}}. \qquad \text{(Equation 4)}$$

The reported values for the ionic charge in the dark are typically $\lesssim 1\mu C.cm^{-2}$.[14,15,25] Assuming, $\epsilon_r = 24$[35] and $N_0 > 10^{15}cm^{-3}$, this implies that V < 300 mV. Hence, at short

Table 1. Comparison of the Mobile Ion Concentration Predicted by the Three Models Discussed above

Model	Gouy-Chapman 2 Mobile Ions	Debye 2 Mobile Ions	Surface Polarization 1 Mobile Ion
Mobile ion concentration (cm^{-3})	3×10^{11}	6×10^{15}	1×10^{17}

For these calculations, we used the same value of the relative dielectric constant used by Weber et. al. ($\epsilon_r = 62$).[15]

circuit, if we assume $V_{bi} = 1$ V and $V_+ = -V_- = 250$ mV, it follows that 0.5 V will drop within the bulk of the absorber.

However, a simplified version of Equation 3, also called the Debye model,[34] is usually used assuming $V \ll V_T$ (i.e., most of the voltage drops within the bulk).[15,24] In this approach, Equation 3 is linearized:

$$Q_{2\ ions}^{Debye} = \frac{\epsilon_0 \epsilon_r V}{L_D} \qquad \text{(Equation 5)}$$

The second approach assumes that the compensating anions are immobile and their concentration is considered uniform within the absorber. This approach has been used to simulate the impact of mobile ions on the hysteresis,[29,36] transient photocurrent,[14] and reverse bias behavior[6] of perovskite solar cells. However, the only analytical expression available in the literature to measure ion concentrations is that proposed by Richardson et al.[9,37–39] These authors developed a method called the "surface polarization" (SP) theory to semi-analytically solve the Poisson equation. In this approach, the ionic charge at the contacts is obtained by analytically calculating the first integral of the Poisson equation, similarly to the Gouy-Chapman theory but with the condition $n_a(x) = N_0$. This model predicts that the ionic charge is distributed asymmetrically as:

$$Q_{1\ ion}^{SP} = \mathrm{sign}(V) \frac{\epsilon_0 \epsilon_r V_T}{L_D} \left[\exp\left(\frac{V}{V_T}\right) - \frac{V}{V_T} - 1 \right]^{1/2}. \qquad \text{(Equation 6)}$$

Nonetheless, to calculate the electrostatic potential and, therefore, the band diagram of perovskite solar cells one must calculate the second integral of the Poisson equation, which is done numerically in the SP theory. Hence, while Equation 6 correctly predicts the asymmetry of the band diagram, this approach does not allow one to recover the vacancy-depleted and accumulation widths with a simple analytical equation from the measurement of the ionic charge (Q_{ion}).

Now that we have compared the assumptions and limitations of the analytical models used or developed in the perovskite solar cell literature, we would like to demonstrate the importance of selecting the correct model to calculate the mobile ion concentration and compute an accurate band diagram. Weber et al.[15] showed that an applied voltage of 0.5 V induced a 0.4 V voltage drop at the perovskite/ETL interface and the corresponding ionic charge was measured to be 260 nC/cm^2. Using Equations 3, 4, 5, and 6, we can calculate the mobile ion concentrations predicted by the three models afore discussed. The results are shown in Table 1 and clearly reveal that selecting a model over another leads to predicted mobile ion concentrations that differ by 2 to 6 orders of magnitude.

Summary of the Conventional Models' Main Features

Two classes of models have been used in the perovskite solar cell literature. The first class of model assumes that two types of mobile ions migrate within the perovskite absorber, while the second one by Richardson and co-workers is based on one

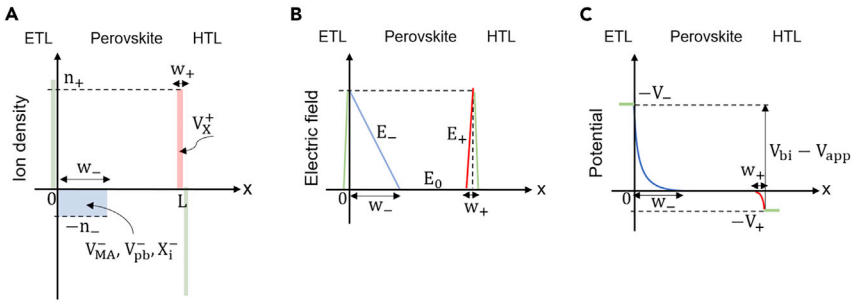

Figure 2. Schematic of the Ion Density, Electric Field, and Electrostatic Potential Profile

(A) Ion density profile in the perovskite absorber at steady state for one type of mobile ion. The density of the electrons and holes accumulating at the contacts, respectively, are shown in green.

(B) Corresponding electric field obtained after integrating the Poisson equation.

(C) Electrostatic potential profile obtained by integrating the electric field distribution of Figure 2B.

single type of mobile ion. The mobile ion concentration that one extracts from measurements varies from 2 to 6 orders of magnitude depending on the selected model used to analyze the data. Hence, it is crucial to use the correct model to accurately extract the mobile ion concentration and compute the solar cell band diagram. The two-mobile-ion model predicts that most of the voltage drops within the bulk of the absorber and is distributed symmetrically at the contacts, unlike what was observed experimentally. This indicates that a 2-mobile ion model cannot be applied to perovskite solar cells. Hence, a one-mobile ion model such as that developed by Richardson et al. is most likely accurate.[9,37–39] However, the approach proposed by these authors requires resorting to complex numerical methods and does not allow one to easily calculate the full band diagram. In the following, we propose an analytical model to quickly recover the full band-diagram based on the migration of one type of mobile ion.

A General Analytical Model

We first state the underlying hypotheses of our model. As in Richardson et al.,[9,37,38] we assume that the compensating anions are immobile (i.e., $n_a = N_0$). However, to find an analytical solution, we make the simplifying assumption that changes in ion concentration take the form of step functions rather than continuous functions. For a given field, vacancies migrate toward the HTL to shield the applied field until a field-free region is created in the bulk of the absorber (when the drift-diffusion current of these mobile vacancies is zero). Concomitantly, the vacancy-depleted region grows wider as vacancies drift toward the HTL. This leads to the asymmetric distribution of Figure 2A.

Case where $w_- + w_+ < L$

Using these hypotheses, we now derive an analytical expression to extract N_0 from the measurement of Q_{ion}. We solve Equations 1 and 2 in the vacancy-depleted (−), neutral (0), and vacancy-accumulation (+) regions (Figure 2A):

$$\begin{cases} \dfrac{\partial E_-}{\partial x} = -\dfrac{q}{\epsilon_0 \epsilon_r} n_- \\ \dfrac{\partial E_0}{\partial x} = 0 \\ \dfrac{\partial E_+}{\partial x} = \dfrac{q}{\epsilon_0 \epsilon_r} n_+ \end{cases} \qquad \text{(Equation 7)}$$

To obtain the electric field in each region, we integrate Equation 7 for each region using the continuity of the electric field and the fact that the field is zero in the neutral region:

$$\begin{cases} E_-(x) = \dfrac{-\partial\phi_-}{\partial x} = -\dfrac{q}{\epsilon_0\epsilon_r} n_-(x - w_-) \\ E_0(x) = -\dfrac{\partial\phi_0}{\partial x} = 0 \\ E_+(x) = -\dfrac{\partial\phi_+}{\partial x} = \dfrac{q}{\epsilon_0\epsilon_r} n_+(x - L + w_+) \end{cases} . \qquad \text{(Equation 8)}$$

The electric field profile is depicted in Figure 2B. The charge neutrality condition imposes that the total ionic charge in the vacancy-depleted region must be equal to that in the vacancy-accumulation region:

$$n_+ w_+ = n_- w_- \qquad \text{(Equation 9)}$$

Equation 9 implies that $E_-(0) = E_+(L)$. We obtain the electrostatic potential by integrating Equation 8, using the continuity of the potential and with the reference potential in the neutral region:

$$\begin{cases} \phi_-(x) = \dfrac{q}{2\epsilon_0\epsilon_r} n_-(x - w_-)^2 \\ \phi_0(x) = 0 \\ \phi_+(x) = -\dfrac{q}{2\epsilon_0\epsilon_r} n_+(x - L + w_+)^2 \end{cases} . \qquad \text{(Equation 10)}$$

The electrostatic potential profile is depicted in Figure 2C. The relation between V_-, V_+, w_- and w_+ is established by using the definition $V_+ - V_- = V_{bi} - V_{app}$ along with Equations 9 and 10 and assuming that the thin vacancy-accumulation region can be assimilated to a Debye layer (Equation 4):

$$\begin{cases} w_+ = L_D = \sqrt{\dfrac{\epsilon_0\epsilon_r V_T}{2qN_0}} \\ V_+ = \dfrac{V_T}{8}\left[\left(1 + 16\dfrac{V_{bi} - V_{app}}{V_T}\right)^{1/2} - 1\right] \\ w_- = \dfrac{L_D}{2}\left[\left(1 + 16\dfrac{V_{bi} - V_{app}}{V_T}\right)^{1/2} - 1\right] \\ V_- = -\dfrac{V_T}{16}\left[\left(1 + 16\dfrac{V_{bi} - V_{app}}{V_T}\right)^{1/2} - 1\right]^2 \end{cases} . \qquad \text{(Equation 11)}$$

In addition, using the fact that $n_- = N_0$, the total charge at the electrodes is given by:

$$Q_{ion} = \pm qN_0 w_- = \pm\frac{1}{4}\frac{\epsilon_0\epsilon_r V_T}{L_D}\left[\left(1 + 16\frac{V_{bi} - V_{app}}{V_T}\right)^{1/2} - 1\right]. \qquad \text{(Equation 12)}$$

Let us remark that away from the flat-band potential (i.e., $V_- \gg V_T$), Equation 12 is asymptotically equivalent to the Equation 6 proposed by Richardson et al., and V_-, w_- and Q_{ion} become

$$\begin{cases} V_- \approx V_{bi} - V_{app} \\ w_- \approx \sqrt{\dfrac{2\epsilon_0\epsilon_r(V_{bi} - V_{app})}{qN_0}} \\ Q_{ion} = \sqrt{2qN_0\epsilon_0\epsilon_r(V_{bi} - V_{app})} \end{cases} . \qquad \text{(Equation 13)}$$

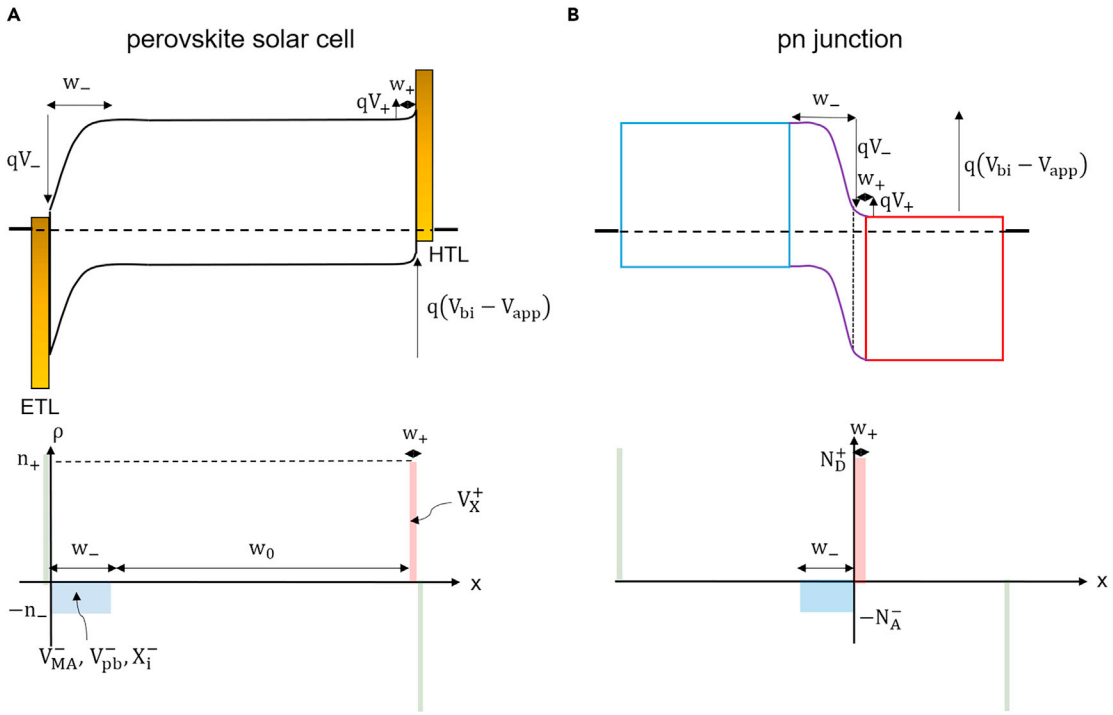

Figure 3. Equilibrium Band Diagram and Ionic Charge Density Profile for Two Solar Devices

(A) A perovskite solar cell, where the band profile is determined by the distribution of accumulating vacancies close to the HTL and the remaining immobile anions in the vacancy-depleted region close to the ETL.

(B) A p-n junction, where the band profile is determined by the distribution of fixed ionized donors and acceptors in the n and p semiconductors, respectively. Note that the charge neutrality condition (Equation 9) imposes that the total charge in the vacancy-depleted and vacancy-accumulation regions is equal. The density of the electrons and holes accumulating at the contacts is shown in green.

The equation defining the vacancy-depleted width in Equation 13 is the same as the equation defining a Schottky barrier and states that most of the potential drops within the region with the lowest ion density (i.e., the vacancy-depleted region). It should also be remarked that in the case where $V_{app} > V_{bi}$, mobile vacancies accumulate at the ETL instead of the HTL and V_{app}, V_{bi}, V_-, V_+, w_-, and w_+ become $-V_{app}$, $-V_{bi}$, V_+, V_-, w_+, and w_-, respectively.

We can now use the electrostatic potential distribution given by Equation 10 and multiply it by the electron charge ($-q$) to plot the energy diagram shown in Figure 3A. As expected, this energy diagram is highly asymmetric and is featured by a field-free region in the bulk of the absorber. A direct analogy can be established with a p-n junction, as shown in Figure 3B. In fact, the vacancy-depleted region in the perovskite solar cell would correspond to a weakly doped p-type semiconductor in a p-n junction, while the vacancy-accumulation region would correspond to a highly doped n-type semiconductor.

Case where $w_- + w_+ = L$

Equations 10, 11, 12, and 13 are valid only if $w_- + w_+ < L$. If $w_- + w_+ \geq L$, this implies that the mobile vacancy concentration is too small to fully shield the potential difference between the ETL and HTL ($V_{bi} - V_{app}$) and the field-free region disappears. The critical vacancy concentration that determines when the electric field is no longer screened in the perovskite bulk is found by solving the equation $w_- + w_+ = L$. For a 400-nm-thick-perovskite device with a voltage drop of 1 V and dielectric constant of 24, this condition is satisfied when $N_0 = 5 \times 10^{15}$ cm^{-3}. Therefore, under these

conditions, mobile vacancy concentrations smaller than 5×10^{15} cm^{-3} will not fully screen the electric field in the bulk of the absorber. In this case, the potential distribution is the sum of the potential due to mobile ion shielding the potential, as defined by Equation 10, and the part of the potential that is not shielded that drops linearly within the absorber. By combining the equation $w_- = L - w_+$ and Equation 11, it follows that Equation 10 becomes

$$\begin{cases} \phi_-(x) = \left[\frac{w_+}{L}\Delta V + \frac{V_T}{4}\left(\frac{L-x}{w_+} - 1\right)\right]\left(\frac{L-x}{w_+} - 1\right) \\ \phi_+(x) = \left[\frac{w_+}{L}\Delta V - \frac{V_T}{4}\left(\frac{L}{w_+} - 1\right)\left(\frac{L-x}{w_+} - 1\right)\right]\left(\frac{L-x}{w_+} - 1\right). \\ \Delta V = V_{bi} - V_{app} - \frac{V_T}{4}\frac{L}{w_+}\left(\frac{L}{w_+} - 1\right) \end{cases} \quad \text{(Equation 14)}$$

Equation 14 is valid only if $w_+ \leq L$. If $w_+ > L$ (which is physically impossible), one must impose $w_+ = L$ in Equation 14. In this case, the potential is not screened and drops linearly within the whole absorber. Using Equation 11, we calculate that for a 400-nm-thick device, the potential is not screened (i.e., when $w_+ = L$) for vacancy concentrations $<10^{14}$ cm^{-3}. To check the accuracy of our model, we compared the potential profile calculated with Equation 10 and that calculated with Equation 14 for low vacancy concentrations to that obtained by solving the full drift-diffusion equations (Figures S2 and S3). Our simulations show that despite the step-function density profiles assumed in our model (Figures 2 and 3), the analytical and numerical solutions are in excellent agreement.

Summary of Our Model's Main Features

Our full analytical model assumes the migration of one type of mobile ion that accumulates at the HTL, in line with studies that show halide vacancies to be the dominant mobile ion in halide perovskites. Note, however, that our model does not preclude the existence of other mobile ions with smaller concentrations[11,20,21] since these ions would not affect the electric field distribution. Our model predicts that if 1V drops within a 400 nm – thick perovskite absorber with a mobile vacancy concentration $>5 \times 10^{15}$ cm^{-3}, most of this voltage drops within the vacancy-depleted region close to the ETL. In the case where negatively charged ions would be mobile instead of positively charged vacancies, the vacancy-depleted region would be formed at the HTL and the accumulation region at the ETL. Our simple model reproduces the field asymmetry and the field-free bulk features discussed in the introduction and can easily be used to extract the mobile vacancy concentrations and the main band diagram features (N_0, w_+, w_-, V_+ and V_-) from charge measurements (Q_{ion}). We point out that this approach is valid to reproduce the electric field even under illumination given that the concentration of free carriers for a working solar cell ($\lesssim 10^{16}$ cm^{-3})[25] is negligible with respect to the ion concentration.

Extraction of Mobile Ion Concentrations in Multiple Perovskite Devices

We now use our model to extract the ion concentration from ionic charge measurements. We measured the ionic charge for 6 different perovskite solar cell compositions. The fabrication process for these devices is detailed in the Experimental Procedures. Note that we tested opaque and semi-transparent (no metal contact) devices and checked that our data was not affected by metal ion diffusion within the absorber.[40,41] As explained in a previous study,[14] we measured Q_{ion} by first letting the devices equilibrate at 0.8 V in the dark. We then removed the applied bias and measured the resulting dark current transient until the cell reached equilibrium steady state at 0 V. By doing so, we could probe the ionic current only since there is

Table 2. Average of the Mobile Vacancy Concentration and Vacancy-Depleted and Vacancy-Accumulation Widths for Perovskite Solar Cells with Different Compositions

Perovskite Composition	PCE(%)	ϵ_r	$N_0(cm^{-3})$	w_- (nm)	w_+ (nm)
$Cs_{0.25}FA_{0.75}Pb(I_{0.80}Br_{0.20})_3$	19.3	24.4	7×10^{16}	211	16
$Cs_{0.17}FA_{0.83}Pb(I_{0.83}Br_{0.17})_3$	17.7	24.2	7×10^{16}	209	16
$MAPbI_3$	13	23.3	4×10^{17}	84	6
$MAPb(I_{0.67}Br_{0.33})_3$	8.7	25.1	3×10^{17}	103	8
$MAPb(I_{0.33}Br_{0.67})_3$	6	26.9	1×10^{17}	155	12
$MAPbBr_3$	3.2	28.7	5×10^{17}	83	6

The power conversion efficiencies (PCEs) are the average PCE for each composition, not the champion PCEs. The dielectric constants were extrapolated from Onoda-yamamuro et al.,[44] and we assumed V_{bi} = 1.2 V.

no electronic injection at 0 V and electronic carriers initially present in the absorbers at 0.8 V are swept away within the first few micro-seconds. By integrating the ionic current during re-equilibration (we removed the fast-electronic capacitive discharge), we could calculate the ionic charge that was moved at the electrodes between 0.8 and 0 V, ΔQ_{ion}, (see Figure S4). With the experimental value of ΔQ_{ion}, we extract N_0 assuming V_{bi} = 1.2 V using Equation 15 (derived using Equation 12):

$$\Delta Q_{ion} = \sqrt{\frac{qN_0\epsilon_0\epsilon_r V_T}{8}}\left[\left(1+16\frac{V_{bi}}{V_T}\right)^{1/2} - \left(1+16\frac{V_{bi}-V_{app}}{V_T}\right)^{1/2}\right]. \quad \text{(Equation 15)}$$

Note that the extracted ion concentration is independent of the value of the initial applied voltage (here V_{app} = 0.8 V), as shown in a previous study.[14] Another way of measuring the mobile ion concentration is to resort to Mott-Schottky experiments, which allow capacitance measurements of the vacancy-depleted region (C_{dl}).[42] Note that the selective contacts are in practice not perfect and part of the voltage drops at the contacts.[15,43] If we assume ~20% of the voltage drops at the contacts, the error on the ion concentration is within ~50% as shown in Figure S5. This error is on the order of the cell to cell variation in Figure S4.

In Table 2, we provide the background ion concentration and the widths of the vacancy-depleted and accumulation regions (w_- and w_+) we measured for each composition. Interestingly, the ion concentrations for all of the cells fall in the same range ($7 \times 10^{16} - 5 \times 10^{17} cm^{-3}$). Note that we have also measured several devices that show vacancy concentrations > $10^{19} cm^{-3}$. However, in general, these devices were fabricated with the p-i-n architecture (instead of the n-i-p architecture reported here) and had low efficiencies. Further investigation is underway to investigate highly efficient devices with different architectures. We remark that the ion concentrations reported here are very similar for perovskite absorbers with and without methylammonium. This suggests that the prevalent mobile ion is not methylammonium but rather halide species (vacancies or interstitials). In addition, for all the compositions, $w_- \sim 83-211$ nm and $w_+ \sim 6-16$ nm. An immediate consequence is that the electric field is confined within 20%– 50% of the absorber and drops linearly (Figure 2B). Therefore, at maximum power point (MPP) for 300- to 500-nm-thick devices, the field in a perovskite solar cell can reach values as high as 8 V/μm at MPP and 55 V/μm at reverse bias (−3 V) at the contacts (Figure S6). In the following, we discuss the implications of this non-uniform and concentrated electric field.

DISCUSSION

In this section, we wish to illustrate the importance of correctly measuring the mobile ion concentration and depicting the band diagram of perovskite solar cells to design

Table 3. Parameters Used for the Simulations of Figures 4, 5, and 6 (Unless Stated Otherwise)

Parameter	Description	Value
ϵ_r	relative permittivity	24 (Van Reenen et al.)[36]
L	device thickness	800 nm (Buin et al.)[45]
N_0	mobile vacancy concentration	$10^{17}cm^{-3}$
n_0, p_0	electron/hole equilibrium densities	4.3×10^{14} cm^{-3}
V_{bi}	built-in potential	1.2V
E_g	band gap energy	1.66 eV (Davies et al.)[46]
μ_n, μ_p	electron/hole mobilities	30 $cm^2V^{-1}s^{-1}$ (Yang et al.)[47]
S_n^{HTL}, S_h^{ETL}	electron and hole surface recombination velocity at the HTL and ETL, respectively	See Table 4
B	bimolecular recombination rate	$5 \times 10^{-10}cm^3s^{-1}$ (Davies et al.)[46]
α	absorption coefficient	2.5×10^4 cm^{-1} (Davies et al.; Chen et al.)[46,48]
Φ_0	photon flux	1.59×10^{17} $s^{-1}cm^{-2}$

efficient and stable devices. In particular, we aim at demonstrating that (1) lower vacancy concentrations are beneficial to devices with large recombination and (2) minimizing surface recombination at the HTL is more important than minimizing surface recombination at the ETL. To support this discussion, we provide a newly designed open-access platform to simulate the band diagram of any perovskite devices .[31] For the simulations presented in this discussion, we used the parameters of Table 3 (unless stated otherwise).

Lower Mobile Ion Concentration Limits the Detrimental Impact of Recombination

Let us first qualitatively explain in which case mobile vacancies are expected to affect the device efficiency. Mobile halide vacancies control the band bending within the absorber but are not necessarily trap states/recombination centers since their energy level is thought to be outside the absorber band gap.[45,49] The band bending (and, hence, the ion concentration) in a solar cell enhances charge separation and minimizes bulk/surface recombination. Band bending increases as the voltage drop within the device in operation is larger. The voltage drop within an operating solar cell is given by the difference between the built-in and maximum power point voltages ($V_{bi} - V_{MPP}$). Therefore, smaller values of V_{MPP} should lead to a larger voltage drop during operation. Since the value of V_{MPP} becomes smaller as the recombination rate within the device increases, the band bending (and, hence, the mobile ion concentration) are expected to mostly impact devices with strong recombination.

For state-of-the-art perovskite solar cells, bulk recombination is mostly governed by band to band recombination. This process rate constant has been measured in the range $10^{-10} - 10^{-9}$ cm^3s^{-1}.[46] In addition, surface recombination rates in the range 500 – 2,000 $cm.s^{-1}$ have been measured for perovskite films.[47,48] These surface recombination rates are 2 to 3 orders of magnitude smaller than for the conventional silicon solar cells.[50] However, since the PL efficiency of perovskite films with contacts is known to be lower, the surface recombination velocities must be higher in devices. For the values of the bulk and surface recombination rates mentioned above, the band bending (and, hence, the mobile ion concentration) should not affect the device efficiency. However, to date the single-junction perovskite solar cells that are studied within the community have efficiencies that span from 15% to 25%[1] and most published devices have efficiencies lower than 20%. Hence, in many devices

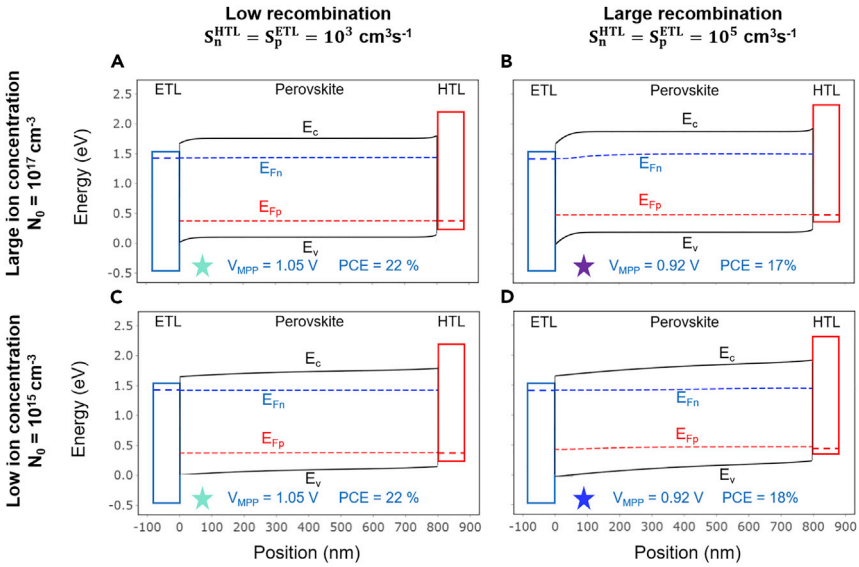

Figure 4. Impact of Recombination on the Device Band Diagram when Illuminating from the ETL

The colored stars are used to locate the recombination conditions on the map of Figure 5. The code for these simulations can be found at https://github.com/LBerto/Joule_Paper_Codes.

the bulk and surface recombination rates may be considerably larger than those mentioned above. In addition, perovskite devices degrade over time and these recombination rates may significantly increase. Hence, it is crucial to quantify how the mobile ion concentration affects the efficiency of devices with recombination rates that are a few orders of magnitudes larger than the rates previously mentioned.

In Figure 4, we provide the band diagrams of perovskite solar cells at the maximum power point in the case where the surface recombination velocity is identical at both contacts for two values of the mobile vacancy concentration (10^{15} and 10^{17} cm^{-3}). In the following, we define B to be the band to band recombination rate and S^h_{ETL} and S^e_{HTL} to be the hole and electron recombination velocities at the ETL and HTL, respectively. For all plots in Figure 4, V_{bi} = 1.2 V and B = 5 × 10^{-10} cm^3s^{-1}. In the case of Figures 4A and 4C, $S^h_{ETL} = S^e_{HTL} = 10^3$ $cm.s^{-1}$ and the resulting value of V_{MPP} is 1.05 V. This implies a 0.15V drop within the absorber. In the case of Figures 4B and 4D, $S^h_{ETL} = S^e_{HTL} = 10^5$ $cm.s^{-1}$ and V_{MPP} = 0.92 V. Hence, a 0.28 V drop occurs within the absorber, unlike 0.15 V in the case of Figures 4A and 4C. This larger voltage drop due to increased recombination current makes the device performance more sensitive to changes in mobile ion concentration. To further understand how the vacancy concentration affects the efficiency of the solar cell, we quantify the surface and bulk recombination currents for each band diagram of Figure 4 (see Table 4).

We first calculate the hole (p(0)) and electron (n(L)) densities at the ETL and HTL, respectively. This allows us to calculate the surface recombination current at the ETL and HTL: $J^h_{ETL} = qS^h_{ETL}p(0)$ and $J^e_{HTL} = qS^e_{HTL}n(L)$. We also calculate the bulk recombination current by integrating the recombination current rate over the whole absorber thickness ($J_{bulk} = \int qB(np - n_i^2)dx$). The total current at the maximum power point (J_{MPP}) is then the difference between the maximum achievable photocurrent due to pure electron/hole photogeneration (J_G) and the surface and bulk recombination currents ($J_{MPP} = J_G - J^h_{ETL} - J^e_{HTL} - J_{bulk}$). As expected, in the case of low recombination

Table 4. Carrier Densities, Generation, and Recombination Current Densities Corresponding to the Band Diagrams of Figure 4

	Figure 4A	Figure 4B	Figure 4C	Figure 4D
N_0 (cm^{-3})	10^{17}	10^{17}	10^{15}	10^{15}
S^h_{ETL}, S^e_{HTL}($cm.s^{-1}$)	10^3	10^5	10^3	10^5
p(0) (cm^{-3})	1.2×10^{12}	1.3×10^{10}	1.4×10^{12}	7.1×10^{10}
n(L) (cm^{-3})	1.7×10^{12}	1.7×10^{11}	1.3×10^{12}	3.7×10^{10}
J^h_{ETL} ($mA.cm^{-2}$)	0.2	0.2	0.2	1.2
J^e_{HTL} ($mA.cm^{-2}$)	0.3	2.8	0.2	0.6
J_{bulk} ($mA.Cm^{-2}$)	6×10^{-3}	5×10^{-4}	5×10^{-4}	10^{-4}
J_G ($mA.cm^{-2}$)	21.3	21.3	21.3	21.3
J_{MPP} ($mA.Cm^{-2}$)	20.8	18.3	20.9	19.5

For these calculations, we used the same value of the relative dielectric constant used by Weber et al. ($\epsilon_r = 62$).[15]

(Figures 4A and 4C), the recombination current is mostly independent of the ion concentration, unlike in the case of larger recombination (Figures 4B and 4D). The dependence of the recombination current on the ion concentration in the case of Figures 4B and 4D relies on the degree of asymmetry of the band diagram. When $N_0 = 10^{17}cm^{-3}$, the asymmetry of the band diagram leads to asymmetric surface recombination currents at the contacts despite the equal surface recombination velocities. More specifically, since most of the band bending occurs close to the ETL, the voltage drop at the perovskite/HTL interface is too small to push electrons away from that interface, leading to higher recombination at the HTL. On the contrary, when $N_0 = 10^{15}$ cm^{-3}, the asymmetry of the band bending vanishes and the voltage drops within the whole device. As a result, the electron density at the HTL is three times lower than in the case where $N_0 = 10^{17}cm^{-3}$. Hence, in the case of strong surface recombination (Figure 4D), the total recombination current is about 1 mA/cm^2 larger than in the case $N_0 = 10^{17}$ cm^{-3} (Figure 4B). Note that the bulk recombination current also decreases by a factor of 5–10. This is why the mobile ion concentration does not affect the device performance in the case of Figures 4A and 4C, while the efficiency differs by 1 point in the case of Figures 4B and 4D. Therefore, our analysis reveals that smaller values of the mobile vacancy concentration are expected to limit recombination.

We now generalize our analysis to a broader range of surface and bulk recombination. In Figure 5, we show two maps of a perovskite solar cell efficiency as a function of the surface and bulk recombination rates for two cases: $N_0 = 10^{17}cm^{-3}$ (Figure 5A) and $N_0 = 10^{15}cm^{-3}$ (Figure 5B). As expected, for devices with larger efficiencies (PCE$\gtrsim$20%), the mobile ion concentration does not impact the solar cell efficiency. In addition, our simulations show that to achieve a 25% efficient solar cell, the band to band recombination rate must be $\lesssim 10^{-10}$ cm^3s^{-1} and the surface recombination velocity at the contacts must be $\lesssim 1$ cms^{-1}. However, for devices with efficiency <20%, the mobile ion concentration does impact the device performance. More specifically, if the band to band recombination rate is $\gtrsim 10^{-7}$ cm^3s^{-1} and/or the surface recombination velocity is $\gtrsim 10^4$ $cm{\cdot}s^{-1}$, multiple efficiency points can be lost by having a mobile ion concentration of $10^{17}cm^{-3}$ instead of $10^{15}cm^{-3}$.

Perovskite Solar Cells Are More Sensitive to Recombination at the HTL than the ETL

So far, we have considered the case of illumination from the ETL and equal surface recombination velocities at both contacts. In Figure 6, we examine the impact of the

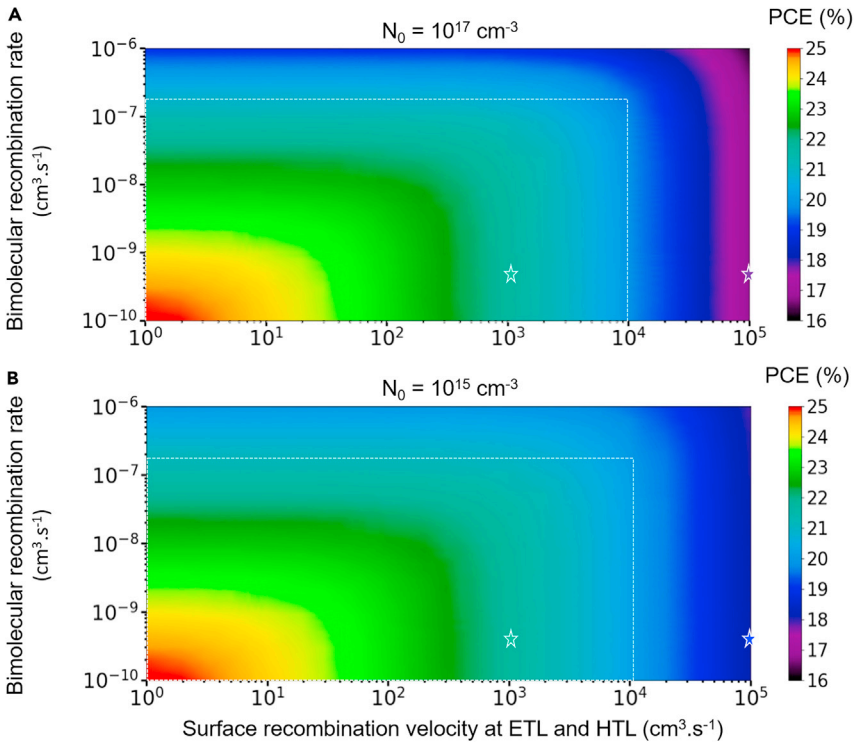

Figure 5. Impact of Surface and Bulk Recombination on the Device Efficiency and Band Diagram Perovskite Solar Cells Illuminated from the ETL

For these simulations the surface recombination velocity is assumed equal at the ETL and HTL. The dotted rectangles correspond to the limit between the cases where the mobile ion concentration does not affect the solar cell efficiency (inside the frame) and the cases where it does (outside the frame). The 4 stars indicate the recombination conditions used for Figures 4A–4D. The simulation parameters are those provided in Table 3. More details about these simulations are provided in the Supplemental Experimental Procedures. The code for these simulations can be downloaded at the following link: https://github.com/LBerto/Joule_Paper_Codes.

illumination side and different surface recombination velocities at the HTL and ETL. For devices with a surface recombination rate of 1,000 cm.s^{-1}, the mobile ion concentration does not affect the device efficiency (orange line). However, when the surface recombination increases by two orders of magnitude, the impact of the mobile ion concentrations differs if surface recombination occurs at the ETL or HTL. In the case of strong hole recombination at the ETL (blue lines), the voltage drop within the whole absorber at lower vacancy concentrations (Figures 4C and 4D) or close to the ETL at larger vacancy concentrations (Figures 4A and 4B) reduces the hole concentration at this interface. Hence the mobile vacancy concentration should affect the relative PCE by less than 5% in the case of hole recombination at the ETL, as shown in Figure 6. On the contrary, the ~100 mV—voltage—drop at the perovskite/HTL interface in the case of larger vacancy concentration (Figures 4A and 4B) will limit surface recombination to a lesser extent than in the case of lower vacancy concentration where the voltage drops throughout the whole device (Figures 4C and 4D). Therefore, the relative PCE can be ~20% lower with vacancy concentrations of 10^{17} cm^{-3} than with concentrations of 10^{15} cm^{-3}, depending on the illumination side, as shown in Figure 6.

Main Takeaways and Implications

Our analysis reveals three important takeaways. First, lower vacancy concentrations ($\lesssim 10^{15}$ cm^{-3}) are beneficial to limit the impact of mobile ions on recombination. This

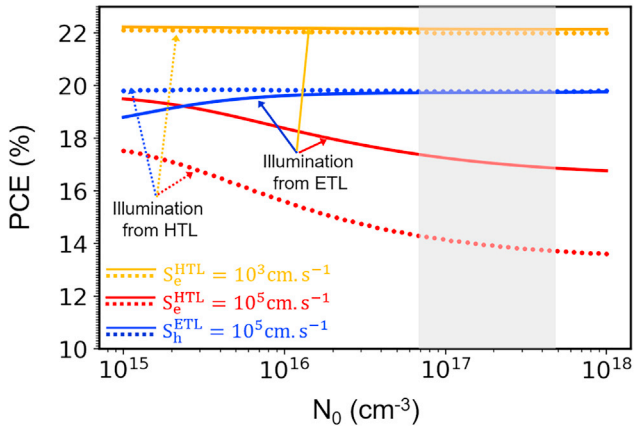

Figure 6. Simulation of the Impact of the Mobile Vacancy Concentration on the PCE of Perovskite Solar Cells as a Function of the Illumination Side

The simulation parameters are the same as those used for the simulations of Figure 4. The gray area indicates the mobile ion concentration range reported in Table 2. The code for these simulations can be found at https://github.com/LBerto/Joule_Paper_Codes.

is consistent with the results of Table 2, which show that the devices with the lowest mobile ion concentrations are the most efficient. This result is also consistent with the suggestion that the addition of excess halide (using potassium iodide for example)[51] or small ions such as cadmium[52] reduces the number of mobile halide vacancies. These treatments have been reported to increase the efficiency by ~ 20% to 40% and/or lead to more stable devices. Second, surface recombination at the HTL can lead to a PCE ~20% lower than surface recombination at the ETL. Hence, concentrating efforts on minimizing recombination at the HTL will lead to a larger increase in efficiency than minimizing surface recombination at the ETL (Figure S7). Finally, there will tend to be less recombination in devices that are illuminated through the side that contains the vacancy-depleted region (the ETL side for positively charged mobile halide vacancies). Since state-of-the-art perovskite solar cells are illuminated through the ETL, our modeling explains why n-i-p cells tend to be more efficient than p-i-n cells.[53–55]

It should be remarked that in this discussion we have only considered the electrostatic aspect of mobile vacancy migration and accumulation at the contacts. However, the concentrated electric field at the contacts also leads to hole accumulation at the perovskite/HTL interface and electron accumulation at the perovskite/ETL interface. Carrier accumulation could lead to chemical reactions with the perovskite absorber and could impact the stability of the perovskite devices.[56] For example, Maier and coworkers showed that halide perovskites can be photo-oxidized by photogenerated holes.[17] Petrozza and coworkers[57] showed that halide photo-oxidation leads to the formation of trap states. In addition, Belisle et al. suggested that this type of process can trigger photo-induced halide segregation and to subsequent quasi-reversible performance losses.[8] Bowring et al. also explained that high electric fields at reverse bias could trigger chemical reactions and a quasi-reversible efficiency drop.[6] Therefore, to fully explain the (photo)-stability of perovskite solar cells, the electrochemical component will have to be considered in addition to the electrostatic component.

Conclusions

We have proposed a full analytical model based on an approach similar to the conventional one for modeling p-n junctions. Our model accounts for the asymmetry of the

band diagram and the field-free region recently observed by experiments. Our analytical approach is in excellent agreement with the full drift-diffusion approach and allows easy calculation of the main features of the perovskite solar cell band diagram and the extraction of mobile ion concentrations from measurements. With our newly designed online-open-access platform, we discussed the impact of the mobile vacancy concentration on the solar cell band diagram for different surface/bulk recombination processes. Using additional simulations of the power conversion efficiency, we showed that lower vacancy concentrations mitigate the impact of bulk/surface recombination and yield larger device efficiencies. In addition, we showed that for the mobile ion concentrations reported in this paper, minimizing surface recombination at the HTL will yield a larger efficiency increase than minimizing surface recombination at the ETL.

EXPERIMENTAL PROCEDURES

Device Fabrication Method

The $Cs_{0.17}FA_{0.83}Pb(I_{0.83}Br_{0.17})_3$ fabrication method can be found in Bush et al.[58] The fabrication method for the $Cs_{0.25}FA_{0.75}Pb(I_{0.8}Br_{0.2})_3$ device will be disclosed in a future publication. In the following, we provide the fabrication method for the $MAPb(I_xBr_{1-x})_3$ devices. ITO-glass slides 10 Ω/square were purchased from Xin Yan Technologies and cleaned with sequential ultrasonic baths containing Extran 300 detergent, DI water, acetone, and isopropanol before dried with N_2 and placed in a UV-ozone cleaner for >15 min. NiO was deposited using an ultrasonic spray coater (AccuMist, Sono-Tek Corporation) operating at 1.0 W and fed by a syringe pump delivering 50 μL/min from an aqueous solution of 20 mM $NiNO_3$ (Sigma) in air at 300°C. The perovskite precursors for $MAPbI_3$ used methylammonium iodide (MAI, Dyesol) and lead iodide (PbI_2, TCI), while $MAPbBr_3$ used methylammonium bromide (MABr, Dyesol) and lead bromide ($PbBr_2$, TCI). In both cases, solutions were made with a 1 M concentration containing 4:1 DMF:DMSO v/v and the perovskite formed in a glovebox with spin coating at 4,000 rpm for 16 s with N_2 flow directed onto the sample for the last 8 s. Mixed halide solutions were obtained by combining the $MAPbI_3$ and $MAPbBr_3$ precursor solutions at appropriate ratios and the perovskite formed with spin coating at 1,000 rpm for 10 s followed by 6,000 rpm for 45 s and then 1,000 rpm for 5.5 s with N_2 flow directed onto the sample for the last 5.5 s. In all cases, the perovskite was formed by annealing on a hot plate for 30 min. For opaque devices, 45 nm of C_{60} (MER Corp.), 7.5 nm of bathocuproine (BCP, TCI), and 150 nm of Ag was sequentially evaporated onto the perovskite. For semi-transparent devices, 30 nm of C60 (MER Corp.) was thermally evaporated (Angstrom Amod), followed by ALD of 6 nm Zn-containing SnO_2[59] (Arradiance GEMStar-6) and 150 nm of DC sputtered ITO (Sunpreme).[60]

Device Characterization

Current-voltage measurements (Figure S8) were obtained with a Keithley 2400 digital source meter. A 300 W xenon lamp (Oriel Sol3A) solar simulator calibrated with a NREL-certified reference photodiode (Newport) was used to irradiate devices from the bottom glass side. jV curves were measured from forward to reverse bias at a 0.1 V s^{-1}. The efficiencies of the highest performing devices are in Table S1.

SUPPLEMENTAL INFORMATION

Supplemental Information can be found online at https://doi.org/10.1016/j.joule.2019.10.003.

ACKNOWLEDGMENTS

This research was supported by the Swiss National Science Foundation "Postdoc Mobility" Fellowship (award number P400P2_180780), the National Science Foundation

Graduate research fellowship (award number DGE-1656518), and the National Science Foundation (award number 1664669). Part of this work was performed at the Stanford Nano Shared Facilities, supported by the National Science Foundation under award ECCS-1542152. We are also grateful to Kevin A. Bush for fruitful discussions, to James A. Raiford and Axel Palmstrom for assistance in depositing the ALD SnO_2 layers, and to Alejandra de la Cruz (janeladra.artstation.com) for drawing the graphical abstract.

AUTHOR CONTRIBUTIONS

L.B. developed and discussed the implications of the model, analyzed the data, and wrote the paper. C.C.B., N.R., and J.X. prepared and characterized the perovskite devices. B.C.O.R. performed the current transient measurements to measure the mobile ion concentration. L.B. and M.D.M. directed and supervised this study.

DECLARATION OF INTERESTS

The authors declare no competing interests.

Received: February 18, 2019
Revised: April 10, 2019
Accepted: October 2, 2019
Published: October 29, 2019

REFERENCES

1. https://www.nrel.gov/pv/cell-efficiency.html.
2. Tress, W. (2017). Metal halide perovskites as mixed electronic-ionic conductors: challenges and opportunities - From hysteresis to memristivity. J. Phys. Chem. Lett. *8*, 3106–3114.
3. Lopez-Varo, P., Jiménez-Tejada, J.A., García-Rosell, M., Ravishankar, S., Garcia-Belmonte, G., Bisquert, J., and Almora, O. (2018). Device physics of hybrid perovskite solar cells: theory and experiment. Adv. Energy Mater. *8*, 1–36.
4. Chen, B., Li, T., Dong, Q., Mosconi, E., Song, J., Chen, Z., Deng, Y., Liu, Y., Ducharme, S., Gruverman, A., et al. (2018). Large electrostrictive response in lead halide perovskites. Nat. Mater. *17*, 1020–1026.
5. Zhao, J., Deng, Y., Wei, H., Zheng, X., Yu, Z., Shao, Y., Shield, J.E., and Huang, J. (2017). Strained hybrid perovskite thin films and their impact on the intrinsic stability of perovskite solar cells. Sci. Adv. *3*, 1–8.
6. Bowring, A.R., Bertoluzzi, L., O'Regan, B.C., and McGehee, M.D. (2018). Reverse bias behavior of halide perovskite solar cells. Adv. Energy Mater. *8*, 1702365.
7. Hoke, E.T., Slotcavage, D.J., Dohner, E.R., Bowring, A.R., Karunadasa, H.I., and McGehee, M.D. (2015). Reversible photo-induced trap formation in mixed-halide hybrid perovskites for photovoltaics. Chem. Sci. *6*, 613–617.
8. Belisle, R.A., Bush, K.A., Bertoluzzi, L., Gold-Parker, A., Toney, M.F., and McGehee, M.D. (2018). Impact of surfaces on photo-induced halide-segregation in mixed-halide perovskites. ACS Energy Lett. *3*, 2694–2700.
9. Richardson, G., O'Kane, S.E.J., Niemann, R.G., Peltola, T.A., Foster, J.M., Cameron, P.J., and Walker, A.B. (2016). Can slow-moving ions explain hysteresis in the current-voltage curves of perovskite solar cells? Energy Environ. Sci. *9*, 1476–1485.
10. Domanski, K., Roose, B., Matsui, T., Saliba, M., Turren-Cruz, S.H., Correa-Baena, J.P., Carmona, C.R., Richardson, G., Foster, J.M., De Angelis, F., et al. (2017). Migration of cations induces reversible performance losses over day/night cycling in perovskite solar cells. Energy Environ. Sci. *10*, 604–613.
11. Eames, C., Frost, J.M., Barnes, P.R.F., O'Regan, B.C., Walsh, A., and Islam, M.S. (2015). Ionic transport in hybrid lead iodide perovskite solar cells. Nat. Commun. *6*, 7497.
12. Calado, P., Telford, A.M., Bryant, D., Li, X., Nelson, J., O'Regan, B.C., and Barnes, P.R.F. (2016). Evidence for ion migration in hybrid perovskite solar cells with minimal hysteresis. Nat. Commun. *7*, 13831.
13. Belisle, R.A., Nguyen, W.H., Bowring, A.R., Calado, P., Li, X., Irvine, S.J.C., McGehee, M.D., Barnes, P.R.F., and O'Regan, B.C. (2017). Interpretation of inverted photocurrent transients in organic lead halide perovskite solar cells: proof of the field screening by mobile ions and determination of the space charge layer widths. Energy Environ. Sci. *10*, 192–204.
14. Bertoluzzi, L., Belisle, R.A., Bush, K.A., Cheacharoen, R., McGehee, M.D., and O'Regan, B.C. (2018). In-situ measurement of electric-field screening in hysteresis-free PTAA/$FA_{.83}Cs_{.17}$ $Pb(I_{.83}Br_{.17})_3$/C_{60} perovskite solar cells gives an ion mobility of $\sim 3 \times 10^{-7}$ cm^2/Vs. J. Am. Chem. Soc. *140*, 12775–12784.
15. Weber, S.A.L., Hermes, I.M., Turren-Cruz, S.H., Gort, C., Bergmann, V.W., Gilson, L., Hagfeldt, A., Graetzel, M., Tress, W., and Berger, R. (2018). How the formation of interfacial charge causes hysteresis in perovskite solar cells. Energy Environ. Sci. *11*, 2404–2413.
16. Yang, T.Y., Gregori, G., Pellet, N., Grätzel, M., and Maier, J. (2015). The significance of ion conduction in a hybrid organic-inorganic lead-iodide-based perovskite photosensitizer. Angew. Chem. Int. Ed. *54*, 7905–7910.
17. Kim, G.Y., Senocrate, A., Yang, T.Y., Gregori, G., Grätzel, M., and Maier, J. (2018). Large tunable photoeffect on ion conduction in halide perovskites and implications for photodecomposition. Nat. Mater. *17*, 445–449.
18. Haruyama, J., Sodeyama, K., Han, L., and Tateyama, Y. (2015). First-principles study of ion diffusion in perovskite solar cell sensitizers. J. Am. Chem. Soc. *137*, 10048–10051.
19. Mosconi, E., and De Angelis, F. (2016). Mobile ions in organohalide perovskites: interplay of electronic structure and dynamics. ACS Energy Lett. *1*, 182–188.
20. Azpiroz, J.M., Mosconi, E., Bisquert, J., and De Angelis, F. (2015). Defect migration in methylammonium lead iodide and its role in perovskite solar cell operation. Energy Environ. Sci. *8*, 2118–2127.
21. Walsh, A., Scanlon, D.O., Chen, S., Gong, X.G., and Wei, S.H. (2015). Self-regulation mechanism for charged point defects in hybrid halide perovskites. Angew. Chem. Int. Ed. *54*, 1791–1794.
22. Ming, W., Chen, S., and Du, M.H. (2016). Chemical instability leads to unusual chemical-potential-independent defect formation and diffusion in perovskite solar cell material $CH_3NH_3PbI_3$. J. Mater. Chem. A *4*, 16975–16981.
23. Mosconi, E., Meggiolaro, D., Snaith, H.J., Stranks, S.D., and De Angelis, F. (2016). Light-induced annihilation of Frenkel defects in organo-lead halide perovskites. Energy Environ. Sci. *9*, 3180–3187.

24. Almora, O., Zarazua, I., Mas-Marza, E., Mora-Sero, I., Bisquert, J., and Garcia-Belmonte, G. (2015). Capacitive dark currents, hysteresis, and electrode polarization in lead halide perovskite solar cells. J. Phys. Chem. Lett. *6*, 1645–1652.

25. Birkhold, S.T., Precht, J.T., Giridharagopal, R., Eperon, G.E., Schmidt-Mende, L., and Ginger, D.S. (2018). Direct observation and quantitative analysis of mobile Frenkel defects in metal halide perovskites using scanning Kelvin probe microscopy. J. Phys. Chem. C *122*, 12633–12639.

26. Yuan, Y., Chae, J., Shao, Y., Wang, Q., Xiao, Z., Centrone, A., and Huang, J. (2015). Photovoltaic switching mechanism in lateral structure hybrid perovskite solar cells. Adv. Energy Mater. *5*, 1–6.

27. Senocrate, A., Moudrakovski, I., Acartürk, T., Merkle, R., Kim, G.Y., Starke, U., Grätzel, M., and Maier, J. (2018). Slow CH_3NH_3+ Diffusion in $CH_3NH_3PbI_3$ under light measured by solid-state NMR and tracer diffusion. J. Phys. Chem. C *122*, 21803–21806.

28. Egger, D.A., Kronik, L., and Rappe, A.M. (2015). Theory of hydrogen migration in organic-inorganic halide perovskites. Angew. Chem. Int. Ed. *54*, 12437–12441.

29. Jacobs, D.A., Wu, Y., Shen, H., Barugkin, C., Beck, F.J., White, T.P., Weber, K., and Catchpole, K.R. (2017). Hysteresis phenomena in perovskite solar cells: the many and varied effects of ionic accumulation. Phys. Chem. Chem. Phys. *19*, 3094–3103.

30. Walter, D., Fell, A., Wu, Y., Duong, T., Barugkin, C., Wu, N., White, T., and Weber, K. (2018). Transient photovoltage in perovskite solar cells: interaction of trap-mediated recombination and migration of multiple ionic species. J. Phys. Chem. C *122*, 11270–11281.

31. https://lucabertoluzzi.shinyapps.io/band_diagram_PSC/.

32. Richter, J.M., Abdi-Jalebi, M., Sadhanala, A., Tabachnyk, M., Rivett, J.P.H., Pazos-Outón, L.M., Gödel, K.C., Price, M., Deschler, F., and Friend, R.H. (2016). Enhancing photoluminescence yields in lead halide perovskites by photon recycling and light out-coupling. Nat. Commun. *7*, 13941.

33. Neukom, M.T., Züfle, S., Knapp, E., Makha, M., Hany, R., and Ruhstaller, B. (2017). Why perovskite solar cells with high efficiency show small IV-curve hysteresis. Sol. Energy Mater. Sol. Cells *169*, 159–166.

34. Butt, H.-J., Graf, K., and Kappl, M. (2003). Physics and Chemistry of Interfaces (Wiley-VCH), p. 13.

35. Brivio, F., Butler, K.T., Walsh, A., and Van Schilfgaarde, M. (2014). Relativistic quasiparticle self-consistent electronic structure of hybrid halide perovskite photovoltaic absorbers. Phys. Rev. B *89*, 1–6.

36. Van Reenen, S., Kemerink, M., and Snaith, H.J. (2015). Modeling anomalous hysteresis in perovskite solar cells. J. Phys. Chem. Lett. *6*, 3808–3814.

37. O'Kane, S.E.J., Richardson, G., Pockett, A., Niemann, R.G., Cave, J.M., Sakai, N., Eperon, G.E., Snaith, H.J., Foster, J.M., Cameron, P.J., et al. (2017). Measurement and modelling of dark current decay transients in perovskite solar cells. J. Mater. Chem. C *5*, 452–462.

38. Courtier, N.E., Cave, J.M., Foster, J.M., Walker, A.B., and Richardson, G. (2019). How transport layer properties affect perovskite solar cell performance: insights from a coupled charge transport/ion migration model. Energy Environ. Sci. *12*, 396–409.

39. Courtier, N.E., Foster, J.M., O'Kane, S.E.J., Walker, A.B., and Richardson, G. (2019). Systematic derivation of a surface polarisation model for planar perovskite solar cells. Eur. J. Appl. Math. *30*, 427–457.

40. Besleaga, C., Abramiuc, L.E., Stancu, V., Tomulescu, A.G., Sima, M., Trinca, L., Plugaru, N., Pintilie, L., Nemnes, G.A., Iliescu, M., et al. (2016). Iodine migration and degradation of perovskite solar cells enhanced by metallic electrodes. J. Phys. Chem. Lett. *7*, 5168–5175.

41. Boyd, C.C., Cheacharoen, R., Bush, K.A., Prasanna, R., Leijtens, T., and McGehee, M.D. (2018). Barrier design to prevent metal-induced degradation and improve thermal stability in perovskite solar cells. ACS Energy Lett. *3*, 1772–1778.

42. Almora, O., Aranda, C., Mas-Marza, E., and Garcia-Belmonte, G. (2016). On Mott-Schottky analysis interpretation of capacitance measurements in organometal perovskite solar cells. Appl. Phys. Lett. *109*, 173903.

43. Hermes, I.M., Hou, Y., Bergmann, V.W., Brabec, C.J., and Weber, S.A.L. (2018). The interplay of contact layers: how the electron transport layer influences interfacial recombination and hole extraction in perovskite solar cells. J. Phys. Chem. Lett. *9*, 6249–6256.

44. Onoda-yamamuro, N., Matsuo, T., and Suga, H. (1992). Study of $CH_3NH_3PbI_3$ (X = Cl, Br, I). J. Phys. Chem. Solids *53*, 935–939.

45. Buin, A., Comin, R., Xu, J., Ip, A.H., and Sargent, E.H. (2015). Halide-dependent electronic structure of organolead perovskite materials. Chem. Mater. *27*, 4405–4412.

46. Davies, C.L., Filip, M.R., Patel, J.B., Crothers, T.W., Verdi, C., Wright, A.D., Milot, R.L., Giustino, F., Johnston, M.B., and Herz, L.M. (2018). Bimolecular recombination in methylammonium lead triiodide perovskite is an inverse absorption process. Nat. Commun. *9*, 293.

47. Yang, Y., Yan, Y., Yang, M., Choi, S., Zhu, K., Luther, J.M., and Beard, M.C. (2015). Low surface recombination velocity in solution-grown $CH_3NH_3PbI_3$ perovskite single crystal. Nat. Commun. *6*, 1–6.

48. Chen, X., Wang, K., and Beard, M.C. (2019). Ultrafast probe at the interfaces of solar energy conversion materials. Phys. Chem. Chem. Phys. *21*, 16399–16407.

49. Yin, W.J., Shi, T., and Yan, Y. (2014). Unusual defect physics in $CH_3NH_3PbI_3$ perovskite solar cell absorber. Appl. Phys. Lett. *104*.

50. Sabbah, A.J., and Riffe, D.M. (2000). Measurement of silicon surface recombination velocity using ultrafast pump-probe reflectivity in the near infrared. J. Appl. Phys. *88*, 6954–6956.

51. Abdi-Jalebi, M., Andaji-Garmaroudi, Z., Cacovich, S., Stavrakas, C., Philippe, B., Richter, J.M., Alsari, M., Booker, E.P., Hutter, E.M., Pearson, A.J., et al. (2018). Maximizing and stabilizing luminescence from halide perovskites with potassium passivation. Nature *555*, 497–501.

52. Saidaminov, M.I., Kim, J., Jain, A., Quintero-Bermudez, R., Tan, H., Long, G., Tan, F., Johnston, A., Zhao, Y., Voznyy, O., et al. (2018). Suppression of atomic vacancies via incorporation of isovalent small ions to increase the stability of halide perovskite solar cells in ambient air. Nat. Energy *3*, 648–654.

53. Jeon, N.J., Na, H., Jung, E.H., Yang, T.Y., Lee, Y.G., Kim, G., Shin, H.W., Il Seok, S., Lee, J., and Seo, J. (2018). A fluorene-terminated hole-transporting material for highly efficient and stable perovskite solar cells. Nat. Energy *3*, 682–689.

54. Jung, E.H., Jeon, N.J., Park, E.Y., Moon, C.S., Shin, T.J., Yang, T.Y., Noh, J.H., and Seo, J. (2019). Efficient, stable and scalable perovskite solar cells using poly(3-hexylthiophene). Nature *567*, 511–515.

55. Jiang, Q., Zhao, Y., Zhang, X., Yang, X., Chen, Y., Chu, Z., Ye, Q., Li, X., Yin, Z., and You, J. (2019). Surface passivation of perovskite film for efficient solar cells. Nat. Photonics *13*, 460–466.

56. Zhao, L., Kerner, R.A., Xiao, Z., Lin, Y.L., Lee, K.M., Schwartz, J., and Rand, B.P. (2016). Redox chemistry dominates the degradation and decomposition of metal halide perovskite optoelectronic devices. ACS Energy Lett. *1*, 595–602.

57. Motti, S.G., Meggiolaro, D., Barker, A.J., Mosconi, E., Perini, C.A.R., Ball, J.M., Gandini, M., Kim, M., De Angelis, F., and Petrozza, A. (2019). Controlling competing photochemical reactions stabilizes perovskite solar cells. Nat. Photonics *13*, 532–539.

58. Bush, K.A., Frohna, K., Prasanna, R., Beal, R.E., Leijtens, T., Swifter, S.A., and McGehee, M.D. (2018). Compositional engineering for efficient wide band gap perovskites with improved stability to photoinduced phase segregation. ACS Energy Lett. *3*, 428–435.

59. Palmstrom, A.F., Raiford, J.A., Prasanna, R., Bush, K.A., Sponseller, M., Cheacharoen, R., Minichetti, M.C., Bergsman, D.S., Leijtens, T., Wang, H.P., et al. (2018). Interfacial effects of tin oxide atomic layer deposition in metal halide perovskite photovoltaics. Adv. Energy Mater. *8*, 1–10.

60. Bush, K.A., Bailie, C.D., Chen, Y., Bowring, A.R., Wang, W., Ma, W., Leijtens, T., Moghadam, F., and McGehee, M.D. (2016). Thermal and environmental stability of semi-transparent perovskite solar cells for tandems by a solution-processed nanoparticle buffer layer and sputtered ITO electrode. Adv. Mater. *28*, 3937–3943.